Progress In Electromagnetics Research, Vol. 125, 255–272, 2012

SAR IMAGING OF SUICIDE BOMBERS WEARING CONCEALED EXPLOSIVE THREATS

J. A. Martínez-Lorenzo*, F. Quivira, and C. M. Rappaport

The Gordon-CenSSIS, Northeastern University, 360 Huntigton Ave, Suite 302 Stearns Center, Boston, MA 02115, USA

Abstract—This paper deals with the problem of detecting potential suicide bombers wearing concealed metallic and dielectric objects. The data produced by Millimeter-Wave-Radar system, working on a Multiple Frequency-Multiple Transmitters and Multiple Receivers configuration (MF-MTMR), is synthetically generated by an electromagnetic code based on Finite Differences Frequency Domain (FDFD) method. The numerical code provides the scattered field produced by the subject under test, which is later processed by using a multiple bistatic Synthetic Aperture Radar (SAR) algorithm. The blurring effect produced by the Point Spread Function (PSF) in the SAR image is removed by applying a regularized deconvolution algorithm that uses only magnitude information (no phase). Finally, the SAR algorithm and the deconvolution procedure are tested on a person wearing metallic and dielectric objects. The SAR response of dielectric rods is quite different from the metallic pipes. Our algorithm not only distinguishes between cases but also is capable of estimating the dielectric constant of the rods. Each constitutive parameter directly maps to the dielectric constant of explosive compounds, such as TNT or RDX, making feasible the detection of potential suicide bombers.

1. INTRODUCTION

In the increasingly important problem of identifying suicide bombers wearing explosives concealed under clothing, it is essential to detect suspicious individuals at a distance. Systems are being developed which employ multiple sensors to determine the presence of explosives on people, including observing and following individuals with

Received 5 December 2011, Accepted 15 February 2012, Scheduled 28 February 2012

* Corresponding author: José Angel Martínez-Lorenzo (jmartine@ece.neu.edu).

intelligent video, identifying explosive residues or heat signatures on the outer surface of their clothing, or by characterizing explosives using penetrating X-rays [1, 2], terahertz waves [3–5], neutron analysis [6, 7] or Nuclear quadrupole resonance (NQR) [8, 9].

At present, radar is the only modality that can penetrate and sense beneath clothing at a distance of 10 to 50 meters without causing physical harm. Successful SAR imaging of suicide bombers wearing concealed metallic structures has been demonstrated previously by our research group [10–12]. It has been shown that a person without metallic pipes produces an SAR image that contains relatively smooth variation on the pixel intensity across the torso of the subject. A human subject wearing metallic pipes produces an SAR image that contains abrupt variations across the torso, with these variations corresponding to the positions of the metallic pipes. A new great challenge arises when the strong metallic scatters are replaced by a weak dielectric scatters — as is the case of explosive compounds like TNT or RDX. For this particular case, the SAR image is highly corrupted by the Point Spread Function (PSF) response resulting from the radar pulse shape and the angular field of view of the synthetic aperture.

In this paper we propose to solve this problem by applying a deconvolution process, which removes the Point Spread Function (PSF) response from the SAR image. Once the image is cleaned by the deconvolution process, the main differences between the metallic pipes and dielectric rods can be better appreciated. In the case of metallic pipes, the image spot associated with each pipe appears to be closer to the radar than the position of the pipe. In the case of dielectric rods, the associated spot appears farther from the radar than the position of the rod, inside the subject's body. As a result of applying this signal processing algorithms, it is possible not only to detect potential suicide bombers but also estimate the constitutive parameters of the substances they wear under clothing.

The structure of this paper is as follows: Section 2 describes the proposed millimeter wave radar system configuration for detection of potential suicide bombers; Section 3 describes the signal processing algorithm for creating the SAR images when the system works in a Multiple-Frequency-Multiple-Transmitter-Multiple Receivers configuration; Section 4 presents a deconvolution algorithm to remove the PSF response from the SAR image; Section 5 introduce the numerical results for a suicide bomber with and without metallic pipes and dielectric rods; in Section 6 the conclusions and major contributions on the paper are described.

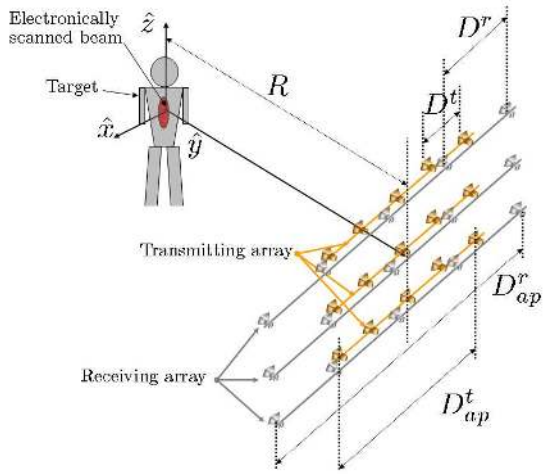

Figure 1. Parameters of the millimeter-wave-radar system.

2. MILLIMETER-WAVE-RADAR SYSTEM FOR SUICIDE BOMBER DETECTION

2.1. System Configuration

The baseline configuration of a Millimeter-Wave-Radar System for Suicide Bomber Detection is depicted in Figure 1. The system is configured to use Multiple-Frequencies and Multiple-Transmitters-Multiple-Receivers (MF-MTMR). The multiple transmitter forms the array in transmission while the multiple receivers form the array in reception. The aperture size of the transmitting and receiving array is D^t_{ap} and D^r_{ap} respectively, and the separation between adjacent elements of the array is D^t in the transmitting array and D^r in the receiving array. Each element of the array in transmission and reception works at multiple frequencies and the total bandwidth of the radar system is BW. The radar system is located at distance R from the subject under test.

For this MF-MTMR configuration, see Figure 2, the field $\mathbf{E}^s\left(f^l, \mathbf{r}^n_t, \mathbf{r}\right)$ scattered by the subject under test is measured by the p-th receiving antenna, which is located at $\mathbf{r} = \mathbf{r}^p_r$ (where $p = 1 \ldots N_p$), when the n-th transmitting antenna, which is located at $\mathbf{r}^n_t$ (where $n = 1 \ldots N_n$), is radiating with the l-th frequency f^l (where $l = 1 \ldots N_l$). Once the scattered field $\mathbf{E}^s\left(f^l, \mathbf{r}^n_t, \mathbf{r}^p_r\right)$ is measured for all transmitting and receiving antennas as well as all frequencies, a SAR algorithm is

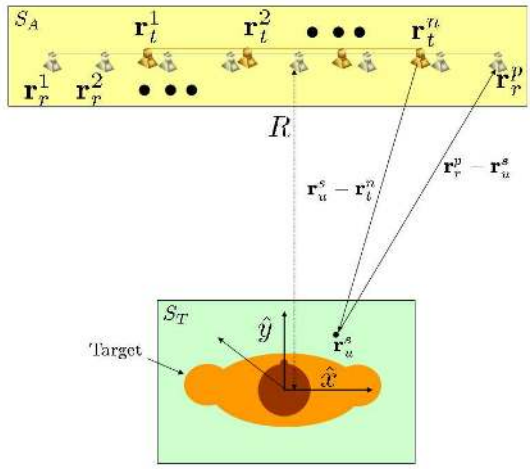

Figure 2. Top view of the geometry configuration and vector notation.

applied in order to generate the images of the subject under test.

In such a MF-MTMR configuration, the amount of information recorded for each transmitting antenna is larger than the one recorded in a Single-Frequency and a moving Single-Transmitter-Single-Receiver (SF-STSR) configuration. Therefore, the expected radar performance of the MF-MTMR is better than the that the SF-STSR configuration, but the system complexity of the former is larger.

2.2. Synthetic Data Generation Using Finite Differences in the Frequency Domain (FDFD)

In order to simulate the electromagnetic behavior of the system, synthetic data is generated by using Finite Differences in the Frequency Domain (FDFD) [16]. This numerical code solves the 2D-Transversal Magnetic (2D-TM) differential equation. Under this configuration, the incident field $\mathbf{E}^i\left(f^l, \mathbf{r}_t^n, \mathbf{r}\right)$ — produced at the region of interest $\mathbf{r} \in S_T$ by the transmitting antenna — and the scattered field $\mathbf{E}^s\left(f^l, \mathbf{r}_t^n, \mathbf{r}\right)$ — generated after the electromagnetic interaction of the incident field and the person under test — are both polarized in the $\hat{\mathbf{z}}$ direction: $\mathbf{E}^i\left(f^l, \mathbf{r}_t^n, \mathbf{r}\right) = E_z^i\left(f^l, \mathbf{r}_t^n, \mathbf{r}\right)\hat{\mathbf{z}}$, and $\mathbf{E^s}\left(f^l, \mathbf{r}_t^n, \mathbf{r}\right) = E_z^s\left(f^l, \mathbf{r}_t^n, \mathbf{r}\right)\hat{\mathbf{z}}$. The relationship between incident and scattered field is governed by the well known 2D-TM wave equation:

$$\left[\nabla_T^2 + k^{l^2}(f^l, \mathbf{r})\right] E_z^s(f^l, \mathbf{r}_t^n, \mathbf{r}) = -\triangle k_p^2(f^l, \mathbf{r}) E_z^i(f^l, \mathbf{r}_t^n, \mathbf{r}) \qquad (1)$$

where the ∇_T^2 is the Laplace operator in the transversal plane, $k^l = 2\pi f^l \sqrt{\mu_0 \epsilon_0 [\epsilon_r(\mathbf{r}) - j\sigma(\mathbf{r})/2\pi f^l \epsilon_0]}$ is the wavenumber, $k_0^l = 2\pi f^l \sqrt{\mu_0 \epsilon_0}$ is the wavenumber in free space, $\triangle k_p^2 = k^{l^2} - k_0^{l^2}$ is the difference between the wavenumber squared and the wavenumber in free space squared, μ_0 and ϵ_0 is the magnetic permeability and dielectric permittivity in free space, ϵ_r is the relative dielectric permittivity, σ is the electrical conductivity, and $j = \sqrt{-1}$. Equation (1) is discretized into pixels, for the region of interest S_T, using a Finite-Difference scheme. For each pixel, the wave number k^l and incident field E_z^i must be specified; so that the scattered field E_z^s is computed by the inversion of a square matrix [16].

3. SYNTHETIC APERTURE RADAR SIGNAL PROCESSING

The two dimensional, phase based MF-MTMR SAR image at the point $\mathbf{r}_u^s$ $(s = 1 \ldots N_s)$ is computed by means of the continuous functional imaging function given by:

$$I(\mathbf{r}_u^s) \doteq K_1 \int_{S_T} h_t(\mathbf{r}, \mathbf{r}_u^s) h_r(\mathbf{r}, \mathbf{r}_u^s) \Upsilon(\mathbf{r}) d\mathbf{r} \tag{2}$$

where $\Upsilon(\mathbf{r})$ represents the objective complex reflectivity function, S_T is a region around the target where the imaging is performed, $h_t(\mathbf{r}, \mathbf{r}_u^s)$ is the field distribution created by the transmitting array when the focusing is performed at the point $\mathbf{r}_u^s$. This function considers the interaction of the electromagnetic wave with the human subject under test, and it is equal to the total field (incident plus scattered) created when the focusing is performed at $\mathbf{r}_u^s$. The function $h_r(\mathbf{r}, \mathbf{r}_u^s)$ is the field distribution that the receiving array would create in transmission when the focusing is performed at $\mathbf{r}_u^s$. This function is based on reception; therefore, there is no interaction with the subject under test. K_1 is a constant that considers amplitude attenuation derived from wave propagation. In the particular case where the array in transmission is modeled as a summation of point sources, and the total field is proportional to the incident field — this is the Born approximation for dielectrics and Physical Optics approximation for perfect electric conductors — the function $h_t(\mathbf{r}, \mathbf{r}_u^s)$ can be approximated by:

$$\begin{aligned} h_t(\mathbf{r}, \mathbf{r}_u^s) &\approx K_2 \sum_n \int_k \int_{S_A} g(k_0) \delta(\mathbf{r}' - \mathbf{r}_t^n) e^{-jk_0(|\mathbf{r}-\mathbf{r}'| - |\mathbf{r}_u^s - \mathbf{r}'|)} d\mathbf{r}' dk_0 \\ &= K_2 \sum_n \int_k g(k_0) e^{-jk_0(|\mathbf{r}-\mathbf{r}_t^n| - |\mathbf{r}_u^s - \mathbf{r}_t^n|)} dk_0 \end{aligned} \tag{3}$$

where $k_0 = 2\pi f\sqrt{\mu_0\epsilon_0}$ is the wave number in free space $-\mu_0$ and ϵ_0 is the permittivity and permeability on the air — $g(k_0)$ is the frequency respond of the radar, S_A is a region containing the transmitting and receiving arrays, K_2 is also a constant which depends on amplitude attenuation derived from wave propagation as well as the boundary conditions of the target. Similarly, the function $h_t(\mathbf{r}, \mathbf{r}_u^s)$ can be approximated by:

$$\begin{aligned} h_r(\mathbf{r}, \mathbf{r}_u^s) &\approx K_3 \sum_p \int_k \int_{S_A} g(k_0)\delta(\mathbf{r}' - \mathbf{r}_r^p) e^{-jk_0(|\mathbf{r}-\mathbf{r}'|-|\mathbf{r}_u^s-\mathbf{r}'|)} d\mathbf{r}' dk_0 \\ &= K_3 \sum_p \int_k g(k_0) e^{-jk_0\left(|\mathbf{r}-\mathbf{r}_r^p|-|\mathbf{r}_u^s-\mathbf{r}_r^p|\right)} dk_0 \end{aligned} \tag{4}$$

where K_3 is a constant which consider amplitude attenuation derived from wave propagation. The discrete version of (2) can be written as [13]:

$$I(\mathbf{r}_u^s) = \sum_{l,n,p} \mathbf{E}(f^l, \mathbf{r}_t^n, \mathbf{r}_r^p) a(f^l, \mathbf{r}_t^n, \mathbf{r}_r^p, \mathbf{r}_u^s) e^{j\Phi(f^l, \mathbf{r}_t^n, \mathbf{r}_r^p, \mathbf{r}_u^s)} \tag{5}$$

where $a(f^l, \mathbf{r}_t^n, \mathbf{r}_r^p, \mathbf{r}_u^s)$ and $\Phi(f^l, \mathbf{r}_t^n, \mathbf{r}_r^p, \mathbf{r}_u^s)$ are the field amplitude attenuation and phase shift associated with a wave propagating from the transmitting antenna $\mathbf{r}_t^n$ to the receiving antenna $\mathbf{r}_r^p$, when the focusing is performed at $\mathbf{r}_u^s$ (see Figure 2). For imaging, the attenuation factor in free space, $a(f^l, \mathbf{r}_t^n, \mathbf{r}_r^p, \mathbf{r}_u^s)$ can be assumed to be constant, since the effect of the phase shift component is dominant.

The phase shift term in (5), when the propagation is in free space, can be written as:

$$\begin{aligned} &\Phi_B^{FS}(f^l, \mathbf{r}_t^n, \mathbf{r}_r^p, \mathbf{r}_u^s) = \phi_1 + \phi_2 \\ &\phi_1 = k_0^l|\mathbf{r}_u^s - \mathbf{r}_t^n|, \quad \phi_2 = k_0^l|\mathbf{r}_r^p - \mathbf{r}_u^s| \end{aligned} \tag{6}$$

where $k_0^l = 2\pi f^l\sqrt{\mu_0\epsilon_0}$ is the wave number in free space (μ_0 and ϵ_0 is the permittivity and permeability on the air). The terms ϕ_1 and ϕ_2 in (6) correspond to the two legs of the path from the transmitter to receiver shown in Figure 2.

A coherent combination of the background field emanating from each transmitting antenna with the first term in (6), ϕ_1, produces a spatially localized spot in transmission around the focusing point $\mathbf{r}_u^s$. The spot has a range resolution of:

$$\Delta R = c/BW \tag{7}$$

where $c = 1/\sqrt{\mu_0\epsilon_0}$ is the propagation speed of the electromagnetic wave in free space. The spot has a cross range resolution of:

$$\Delta R_x \approx \lambda_0 R/D_{ap}^t \tag{8}$$

By reciprocity, the second term in (6), ϕ_2, produces a spatially localized spot in reception around the focusing point.

The field distribution created by the array in transmission, $h_t(\mathbf{r}, \mathbf{r}_u^s)$, contains grating lobes in cross range, which are separated from the desired spatially localized spot — centered at $\mathbf{r}_u^s$ — a distance:

$$L_x^t = R \tan\left(\sin^{-1}\left(\frac{q\lambda}{D^t}\right)\right) \tag{9}$$

where q is an integer taking values different from zero. When the element separation D^t is increased, the grating lobe distance L_x^t is reduced.

The result of sampling the bandwidth BW in N_l samples also produces grating lobes in range with the field distribution function $h_t(\mathbf{r}, \mathbf{r}_u^s)$, which are separated from the desired spatially localized spot a distance:

$$L^t = \frac{c}{BW}(N_l - 1) \tag{10}$$

The field distribution function of the receiving array, $h_r(\mathbf{r}, \mathbf{r}_u^s)$, also contains grating lobes L_x^r and L^r in cross range and range. The equation for L_x^r is the same as (12) with the distance between adjacent elements of the array in transmission D^t is replaced by the distance in reception D^r.

3.1. Point Spread Function Deconvolution from SAR Image

The Point Spread Function (PSF) is approximated using (2) when the reflectivity function, $\Upsilon(\mathbf{r})$, is a point source, $\delta(\mathbf{r})$.

$$\mathrm{PSF}(\mathbf{r}_u^s) = K_1 \int_{S_T} h_t(\mathbf{r}, \mathbf{r}_u^s) h_r(\mathbf{r}, \mathbf{r}_u^s) \delta(\mathbf{r}) d\mathbf{r} = K_1 h_t(0, \mathbf{r}_u^s) h_r(0, \mathbf{r}_u^s) \tag{11}$$

Therefore, SAR image is approximately equal to the complex convolution of the PSF with the reflectivity function.

$$I(\mathbf{r}_u^s) \approx \mathrm{PSF}(\mathbf{r}_u^s) * \Upsilon(\mathbf{r}_u^s) \tag{12}$$

where $*$ indicates the two dimensional complex convolution. In order to better estimate the reflectivity function, the PSF distribution, PSF $(\mathbf{r}_u^s)$, can be deconvolved from the SAR image $I(\mathbf{r}_u^s)$. For this paper we have used the regularized deconvolution algorithm [14, 15], where the magnitude of the PSF is deconvolved from the magnitude of the SAR image. The regularized deconvolution of complex signals must be addressed in future work, as it is beyond the scope of this paper.

4. NUMERICAL RESULTS

4.1. Radar Configuration

The radar configuration used in this paper is summarized in Table 1. Figure 3(a) presents the squared magnitude of the approximation of the field distribution function $h_t(\mathbf{r}, \mathbf{r}_u^s)$ given by (3). The characteristic grating lobes, in both range and cross range, are present at distances $L^{t/r} = 0.7496$ meters and $L_x^t = 0.5459$ meters. Figure 3(b) presents a zoomed version of Figure 3(a) around the main spot. The shape of this spot in cross range is approximately of the form sinc $= \sin(N_n K_4 x)/\sin(K_4 x)$, where K_4 is a constant depending on the wave number and the separation between adjacent elements of the array [18]. The shape of the spot in range is also of the form sinc $= \sin(N_l K_5 Y)/\sin(K_5 Y)$, where K_5 is a constant depending on the sampling period in the frequency domain [19]. This two dimensional distribution results from using uniform amplitude coefficients for exciting every element of the array for each frequency.

Figures 3(c)–(d) present equivalent results for the field distribution function $h_r(\mathbf{r}, \mathbf{r}_u^s)$ given by (4). Since the aperture size of the transmitting array, $D_{ap}^t = 0.7$ meters, is smaller than the aperture size of the receiving array, $D_{ap}^r = 3.2$ meters, the cross range resolution in transmission, $\Delta R_x^t = 0.0454$ meters, is bigger than in reception, $\Delta R_x^r = 0.0099$ meters. The separation between two adjacent elements in the transmitting array is smaller than in the receiving one, therefore the grating lobes in cross range for the former are further apart than for the latter.

Figure 3(e) presents the magnitude of the product of the filed distribution function in transmission and in reception, a as given by (5). The cross range grating lobes of this product which are located at the same range as the main spot are almost zero. This result is a direct consequence of using different separation between adjacent array elements in transmission and in reception. The image distortion effect due to other cross range grating lobes, not coincident with the range of the main spot, can be removed by reducing the sampling frequency of the bandwidth. For this particular case, the depth of the human subject in range is smaller than the distance between adjacent grating lobes in range $L^{t/r} = 0.7496$ [m], therefore there is no image distortion effect present in the SAR images.

4.2. Synthetic Data Generation with the FDFD

The human subject is modeled based on a human cross section obtained from the visible human project [17], which is represented in Figure 4(a).

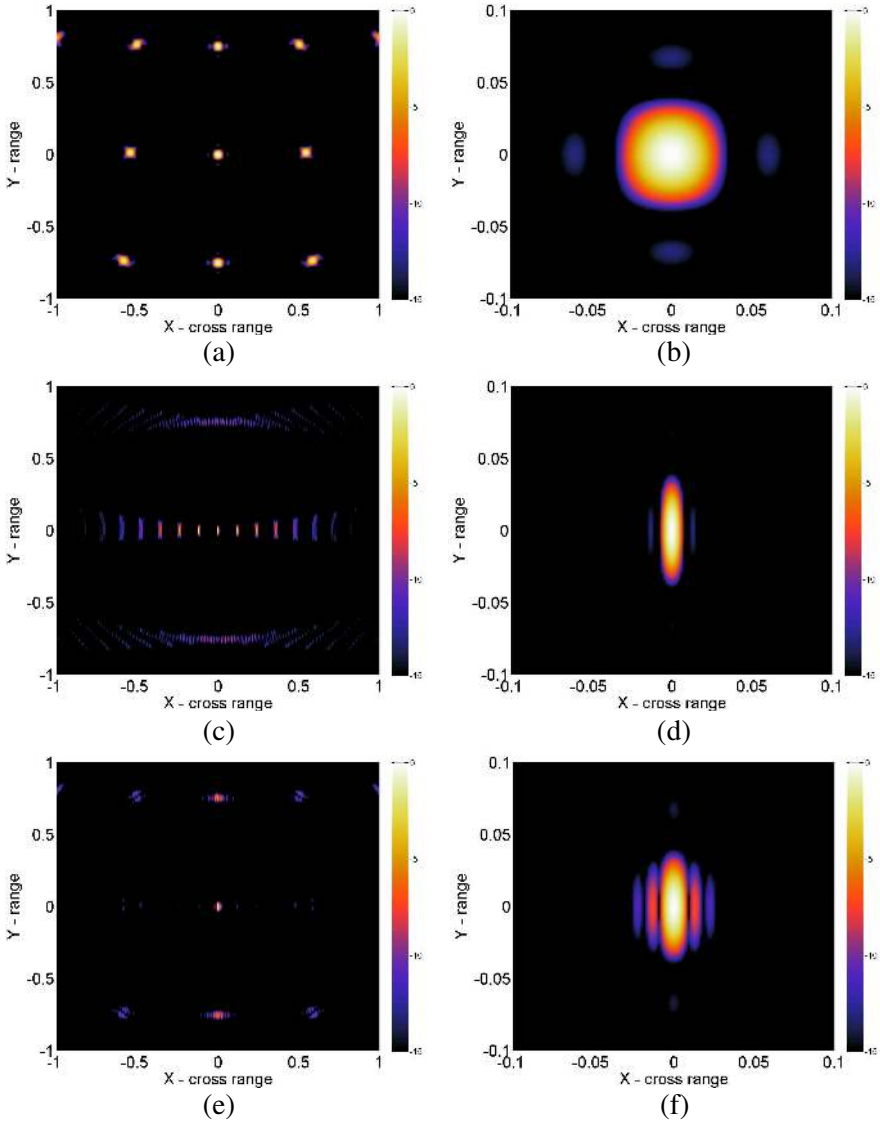

Figure 3. Field distribution function: $|h_t(\mathbf{r}, \mathbf{r}_u^s)|^2$. (a) Wide region, (b) zoomed region; $|h_r(\mathbf{r}, \mathbf{r}_u^s)|^2$, (c) wide region, (d) zoomed region; $|h_t(\mathbf{r}, \mathbf{r}_u^s) h_r(\mathbf{r}, \mathbf{r}_u^s)|$, (e) wide region, (f) zoomed region (color-bars range: 0 to -15 dB).

Table 1. Parameters for the baseline configuration.

RADAR SOURCE	
Center frequency	$f_c = 94.5$ [GHz]
Bandwidth	$BW = 6$ [GHz]
Number of frequencies	$N_l = 8$
Range resolution in air	$\Delta R = 0.0500$ [m]
Grating lobes distance in range	$L^{t/r} = 0.7496$ [m]
TRANSMISSION (equally spaced point sources)	
Number of transmitting antennas	$N_n = 13$
Position in [m] of the first element	$\mathbf{r}_r^1 = -0.35\hat{\mathbf{x}} + 10\hat{\mathbf{y}}$
Position in [m] of the last element	$\mathbf{r}_r^{13} = 0.35\hat{\mathbf{x}} + 10\hat{\mathbf{y}}$
Cross range resolution in air	$\Delta R_x^t = 0.0454$ [m]
Grating lobe distance in cross range	$L_x^t = 0.5459$ [m]
RECEPTION (equally spaced point sources)	
Number of receiving antennas	$N_p = 13$
Position in [m] of the first element	$\mathbf{r}_r^1 = -1.6\hat{\mathbf{x}} + 10\hat{\mathbf{y}}$
Position in [m] of the last element	$\mathbf{r}_r^{13} = 1.6\hat{\mathbf{x}} + 10\hat{\mathbf{y}}$
Cross range resolution in air	$\Delta R_x^r = 0.0099$ [m]
Grating lobe distance in cross range	$L_x^r = 0.1192$ [m]

Different regions of the image are coded into a matrix of indices, see Figure 4(b), which is used by the FDFD code to generate the synthetic data. Free space is represented by a value of one in the image, and the wave number at this region is equal that of a wave propagating in free space $k^l = k_0^l$. Skin is coded by a value of zero, and the wave number at this region is equal to $k^l = k_0^l\sqrt{(11.9 - j55.6/(2\pi f^l \epsilon_0))}$, which is based on extrapolated measured dielectric constant values at W-band.

The FDFD code computes the fields in the first 2 millimeters of conducting high water content skin, and then considers the fields inside the human body to be zero, since the skin at working frequencies is so conductive that waves attenuate more than an order of magnitude by the time they traverse the skin layer. The latter approximation drastically reduces the computational cost of these simulations. Regions in which the total field is zero is coded by a

value of two in the FDFD grid represented in Figure 4(b). Metallic pipes are also coded by a value of two in the image, since the total field is also zero at these regions (see Figure 4(c)). Dielectric rods are easily simulated by adding an index to the grid, indicating a dielectric wave number given by $k^l = k_0^l\sqrt{\epsilon_r}$ (where ϵ_r takes a variety of sample low-loss material values running from 1 to 7.5).

4.3. SAR Imaging and PSF Deconvolution: Suicide Bomber with Metallic Pipes

The SAR images for a person with and without metallic pipes are presented in Figure 5. These images are obtained from a pixel based matrix derived from (6) and the radar pointing normally to the front of a subject's torso. Figure 5(a) shows the case of a person without metal pipes. The pixel intensity across the torso of the subject presents a relatively smooth variation. Figure 5(c) presents the image for a person wearing metal pipes. The pixel intensity across the torso presents abrupt variations mapping to the position of the metallic pipes. These SAR images also show that only the regions where a specular reflection contribution is produced are seen in the image.

Figures 5(b) and 5(d) present the SAR images after applying the deconvolution algorithm. The deconvolution algorithm using only the magnitude of both the PSF and the SAR image produce a better reconstruction of the reflectivity function $\Upsilon(\mathbf{r})$, since the elongation artifacts of the PSF are absent in the new images.

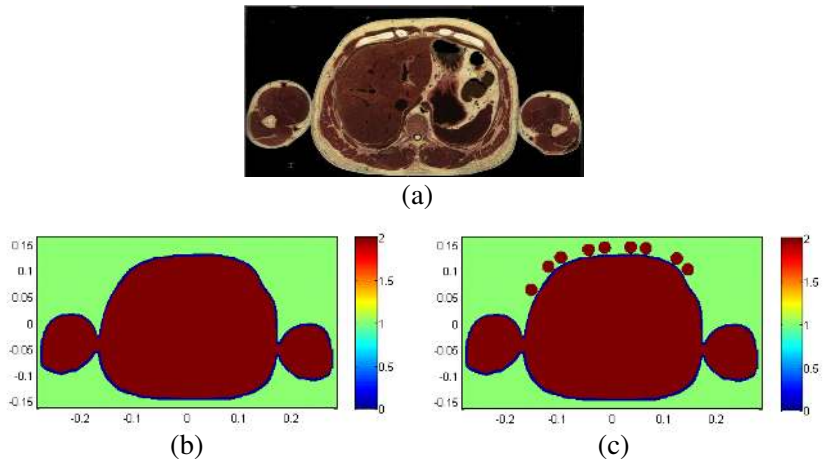

Figure 4. Human body cross section: (a) real image, (b) FDFD model [17], (c) FDFD model with metallic pipes.

4.4. SAR Imaging and PSF Deconvolution: Suicide Bomber with Dielectric Rods

Figures 6–8 present the front part of the human cross section — which contains regions producing specular reflections — and the SAR image after applying deconvolution when the diameter of the rods are 1.5, 2 and 2.5 [cm] and have different dielectric constants.

In the case of metallic pipes, the image spot associated with each pipe appears to be closer to the radar than the position of the pipe. In the case of dielectric rods, the associated spot appears farther from the radar than the position of the rod, inside the subject's body.

The explanation for this effect is that the SAR algorithm images using the free space wavenumber k_0^l in (6), but that the wavenumber for the field propagating through a dielectric rod $-k^l = k_0^l\sqrt{\epsilon_r}$, where ϵ_r is the relative dielectric constant of the rod — is larger than the free space wavenumber. Therefore, the speed of propagation in the dielectric is reduced, and the spot associated with the dominant reflection from the chest is delayed. As expected, when the relative permittivity of the dielectric rod is increased, the velocity is further reduced, and the delay for the chest reflection spot is also increased, making the spot appear deeper into the chest. Finally, it is possible to measure the delay

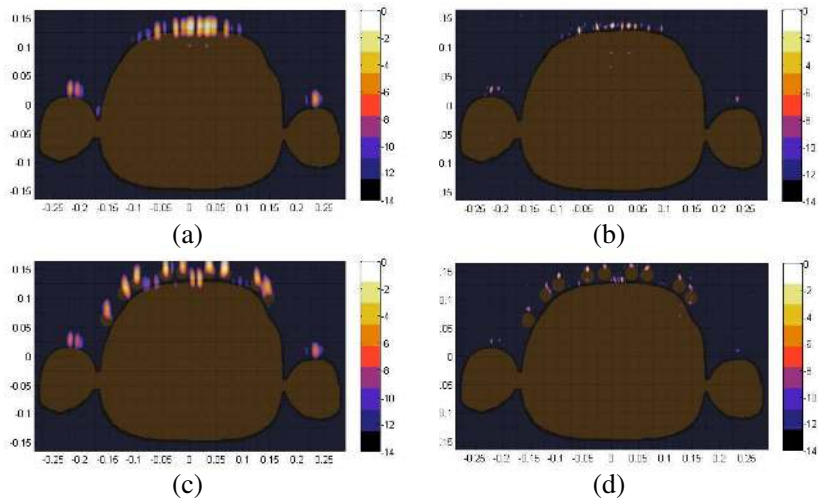

Figure 5. SAR image and cross section of simulated human subject with: no metallic pipes (a) before deconvolution, (b) after deconvolution; metallic pipes (c) before deconvolution, (d) after deconvolution.

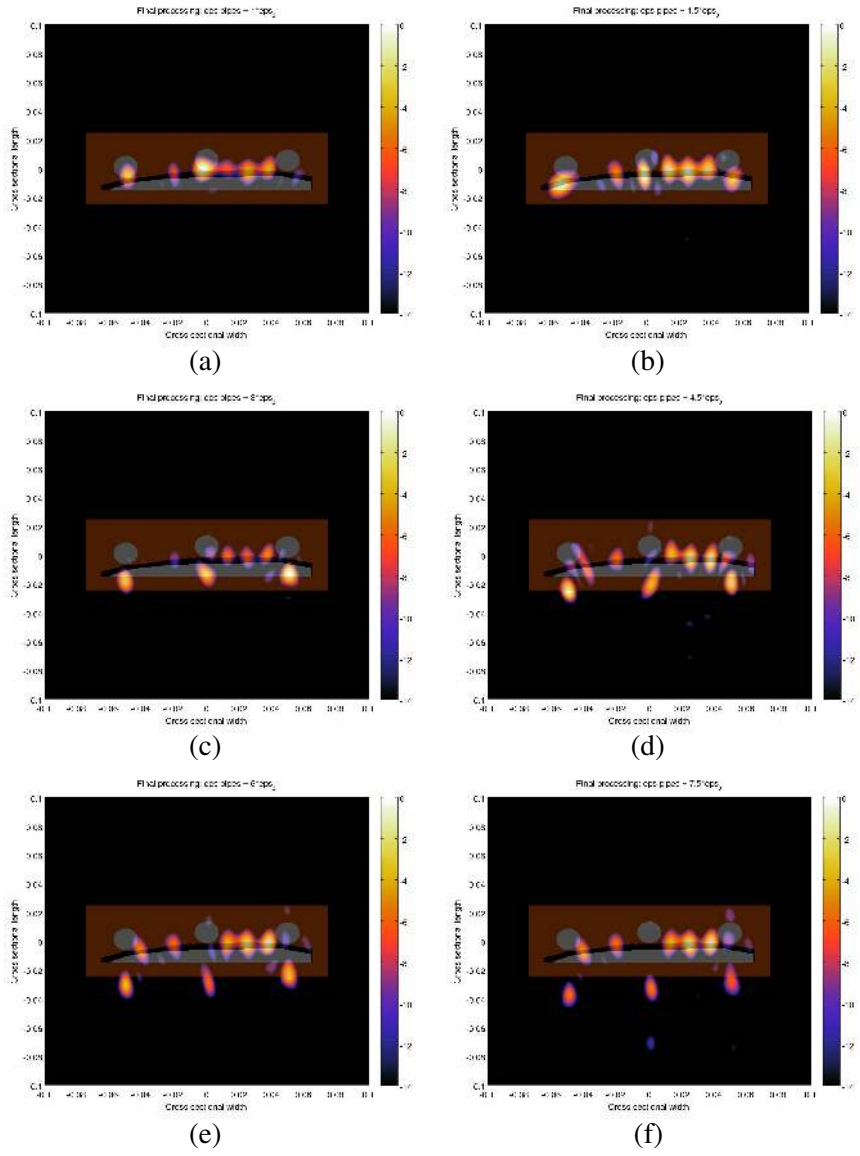

Figure 6. Front part of the simulated human cross section and SAR image after applying deconvolution when the diameter of the rods is 1.5 [cm] and the dielectric constant is: (a) $1\epsilon_0$, (b) $1.5\epsilon_0$, (c) $3\epsilon_0$, (d) $4.5\epsilon_0$, (e) $6\epsilon_0$, (f) $7.5\epsilon_0$ (color-bars range: 0 to -14 dB).

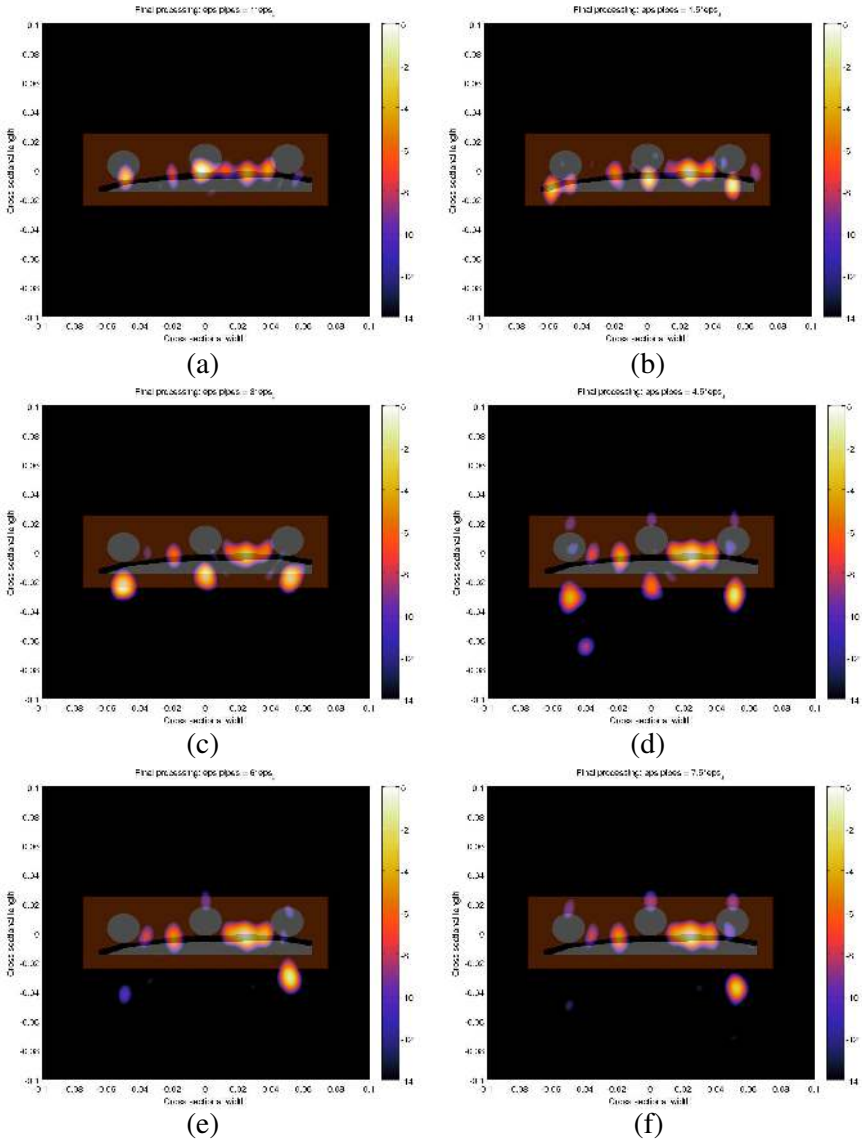

Figure 7. Front part of the simulated human cross section and SAR image after applying deconvolution when the diameter of the rods is 2 [cm] and the dielectric constant is: (a) $1\epsilon_0$, (b) $1.5\epsilon_0$, (c) $3\epsilon_0$, (d) $4.5\epsilon_0$, (e) $6\epsilon_0$, (f) $7.5\epsilon_0$ (color-bars range: 0 to -14 dB).

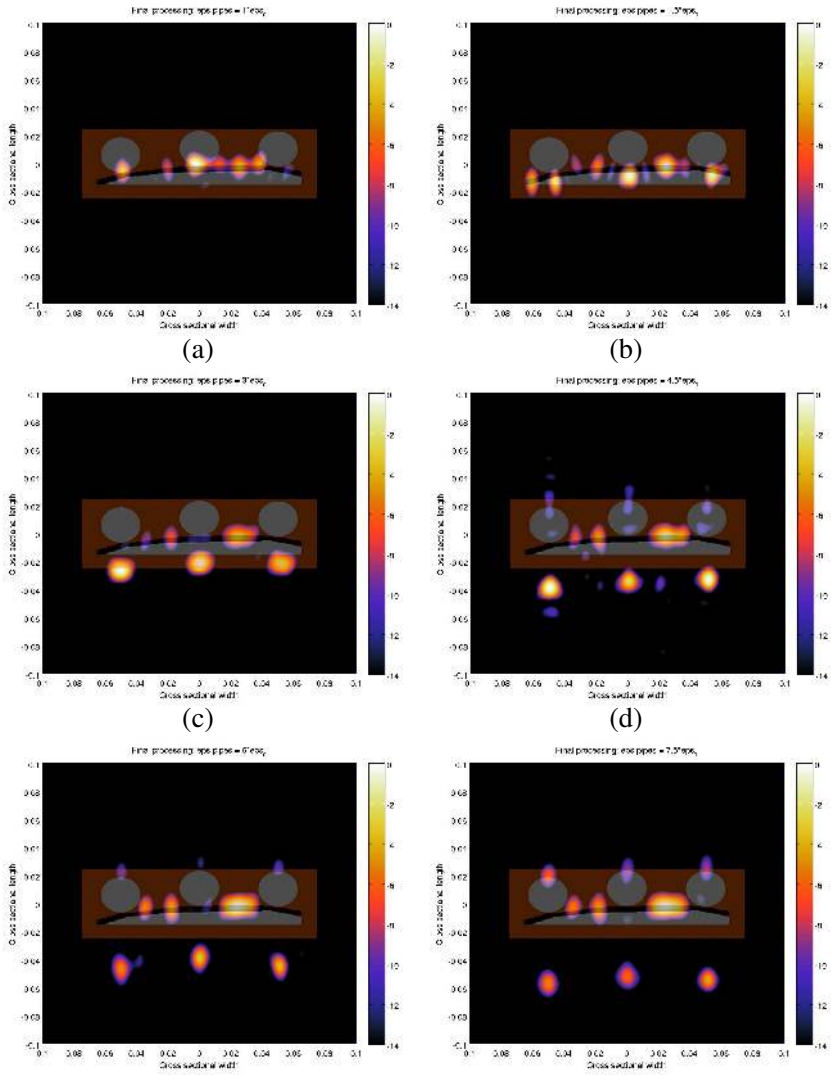

Figure 8. Front part of the simulated human cross section and SAR image after applying deconvolution when the diameter of the rods is 2.5 [cm] and the dielectric constant is: (a) $1\epsilon_0$, (b) $1.5\epsilon_0$, (c) $3\epsilon_0$, (d) $4.5\epsilon_0$, (e) $6\epsilon_0$, (f) $7.5\epsilon_0$ (color-bars range: 0 to -14 dB).

distance as a function of the dielectric permittivity, which can be used to identify the constitutive parameters of the dielectric materials, to further confirm or rule out the presence of explosives. The diameter

of the spot is also proportional to the diameter of the dielectric pipe, therefore it is possible to independently determine both rod's size and dielectric constant.

5. CONCLUSION

This paper has presented a model of a millimeter wave radar system for suicide bomber detection. The system uses different arrays in transmission and in reception, since such a configuration ensures that the grating lobes in cross range of the array in transmission are not coincident with the ones of the array in reception. Therefore, the blurring effect that the grating lobes have in the SAR image is eliminated. The system works in a Multiple Frequency-Multiple Transmitters-Multiple Receivers (MF-MTMR) configuration, requiring the traditional dynamic monostatic SAR imaging algorithm to be modified to work in a multi-static configuration.

The SAR images are highly corrupted by the Point Spread Function (PFS) response of the system. In order to remove the burring effect that the PFS response has on the SAR image, we have proposed a regularized deconvolution algorithm. The new images generated after applying the deconvolution are unbiased with respect of the PSF response, resulting in a better reconstruction of the reflectivity function. For this particular configuration, it has been shown that a deconvolution using only the magnitude of both the SAR image and PSF produce a good reconstruction of the reflectivity function. The deconvolution using the complex valued SAR image and PSF is the subject of future research.

The performance of the MF-MTMR SAR imaging algorithm and the deconvolution process have been tested on simulated human cross sections with and without metallic pipes and dielectric rods. The reflectivity function can only be reconstructed in regions where a specular reflection is produced. As a result, the top part of the metallic pipes are clearly seen in the SAR image as well as the front part of the chest of the human body.

The reflectivity function reconstructed when the human subject is wearing dielectric rods is quite different from when he is wearing metallic pipes. In the case of metallic pipes, all the wave energy is reflected from the front of the pipe, while for the dielectric rods, part of the wave travels through the rod, is reflected on the chest of the subject under test, then travels again through the rod and finally propagates towards the radar. This effect of traveling through a dielectric medium reduces the speed of propagation of the wave when compared with free space propagation, therefore a reflection that should appear to be in

the front of the chest of the human body appears delayed in the SAR image.

Finally, it is possible to measure the delay distance as a function of the dielectric permittivity, and for different diameters of the rod, leading to a function that can be used to identify the constitutive parameters of concealed substances. This information can be compared to the dielectric constants of some well characterized compounds like TNT or RDX, making feasible the detection of potential suicide bombers.

ACKNOWLEDGMENT

This material is based upon work supported by the Science and Technology Directorate, U.S. Department of Homeland Security under the Award Number "2009-ST-108-000009". The views and conclusions contained in this document are those of the authors and should not be interpreted as necessarily representing the official policies, either expressed on implied, of the U.S. Department of Homeland Security.

REFERENCES

1. Yinon, J., "Field detection and monitoring of explosives," *Trends in Analytical Chemistry*, Vol. 21, No. 3, 415–423, 2002.
2. Yinon, J., *Forensic and Environmental Detection of Explosives*, John Wiley and Sons, Chichester, 1999.
3. Leahy-Hoppa, M., M. Fitch, X. Zheng, L. Hayden, and R. Osiander, "Wideband terahertz spectroscopy of explosives," *Chemical Physics Letters*, Vol. 424, No. 8, 227–230, 2007.
4. Cook, D. J., B. K. Decker, and M. G. Allen, "Quantitative THz spectroscopy of explosive materials," *Optical Terahertz Science and Technology*, 14–16, Mar. 2005.
5. Liu, H., Y. Chen, G. J. Bastiaans, and X. Zhang, "Detection and identification of explosive RDX by THz diffuse reflectionspectroscopy," *Optics Express*, Vol. 14, 415–423, 2006.
6. Shea, P., T. Gozani, and H. Bozorgmanesh, "A TNA explosives-detection system in airline baggage," *Nuclear Instruments and Methods in Physics Research Section A: Accelerators, Spectrometers, Detectors and Associated Equipment*, Vol. 299, No. 20, 444–448, Dec. 1990.
7. Fink, C. L., B. J. Micklich, T. J. Yule, P. Humm, L. Sagalovsky, and M. M. Martin, "Evaluation of neutron techniques for illicit substance detection," *Nuclear Instruments and Methods in*

Physics Research Section B: Beam Interactions with Materials and Atoms, Vol. 99, No. 1–4, 748–752, May 1995.

8. Itozaki, H. and G. Ota, "International journal on smart senssing and intelligent system," *Nuclear Quadrupole Resonanace for Explosive Detection*, Vol. 1, No. 3, 705–715, Sep. 2008.
9. Miller, J. B. and G. A. Barral, "Explosives detection with nuclear quadrupole resonance," *American Scientist*, Vol. 93, 50–57, Jan.–Feb. 2005.
10. Martinez-Lorenzo, J. A., C. M. Rappaport, R. Sullivan, and A. Angell, "Standoff concealed explosives detection using millimeter-wave radar to sense surface shape anomalies," *Proc. IEEE AP-S International Symposium, AP-S 2008*, 2008.
11. Valdes, B. G., J. A. Martinez-Lorenzo, C. M. Rappaport, and A. G. Pino, "Design and near field based optimization on an array of reflectors as radar antenna to sense surface shape anomalies," *Proc. IEEE AP-S International, AP-S 2009*, 2009.
12. Fernandes, J., J. A. Martinez-Lorenzo, M. Hagelen, and C. M. Rappaport, "Experimental results for standoff detection of concealed body-worn explosives using millimeter-wave radar and limited view isar processing," *Homeland Security Technology Conference*, 2009.
13. Martinez, J., C. Rappaport, and F. Quivira, "Physical limitations on detecting tunnels using underground focusing synthetic aperture radar," *IEEE Transactions on Geoscience and Remote Sensing*, Vol. 49, No. 1, 65–70, 2011.
14. Jain, A. K., *Fundamentals of Digital Image Processing*, Prentice Hall, New Jersey, 1989.
15. Gonzalez, R. C. and R. E. Woods, *Digital Image Processing*, Addison-Wesley Publishing Company, 1992.
16. Rappaport, C. M., Q. Dong, E. Bishop, A. Morgenthaler, and M. Kilmer, "Finite difference frequency domain (FDFD) modeling of two dimensional te wave propagation and scattering," *URSI Symp. Digest*, May 2004.
17. United States National Library of Medicine, National Institutes of Health, "The visible human project." [Online]. Available: http://www.nlm.nih.gov/research/visible/visible human.html.
18. Balanis, C. A., *Antenna Theory*, Willey and Sons, New Jersey, 2005.
19. Oppenheim, A. V., R. W. Schafer, and J. R. Buck, *Discrete-time Signal Processing*, Prentice Hall, New Jersey, 1999.